

On the aeroacoustic characterization of a robust trailing-edge serration

Cite as: Phys. Fluids **33**, 075120 (2021); <https://doi.org/10.1063/5.0054767>

Submitted: 21 April 2021 • Accepted: 20 June 2021 • Published Online: 23 July 2021

 A. Celik, Y. D. Mayer and  M. Azarpeyvand



View Online



Export Citation



CrossMark

ARTICLES YOU MAY BE INTERESTED IN

[A study of the effect of serration shape and flexibility on trailing edge noise](#)
Physics of Fluids **32**, 127114 (2020); <https://doi.org/10.1063/5.0032774>

[On the noise reduction of a porous trailing edge applied to an airfoil at lifting condition](#)
Physics of Fluids **33**, 055132 (2021); <https://doi.org/10.1063/5.0047512>

[Experimental investigation of the wake dynamics for a NACA0012 airfoil with a cut-in serrated trailing-edge](#)
Physics of Fluids **33**, 055122 (2021); <https://doi.org/10.1063/5.0046318>

APL Machine Learning

Open, quality research for the networking communities

MEET OUR NEW EDITOR-IN-CHIEF

LEARN MORE



On the aeroacoustic characterization of a robust trailing-edge serration

Cite as: Phys. Fluids **33**, 075120 (2021); doi: [10.1063/5.0054767](https://doi.org/10.1063/5.0054767)

Submitted: 21 April 2021 · Accepted: 20 June 2021 ·

Published Online: 23 July 2021



View Online



Export Citation



CrossMark

A. Celik,^{a)}  Y. D. Mayer,^{b)} and M. Azarpeyvand^{c)} 

AFFILIATIONS

University of Bristol, Faculty of Engineering, Bristol BS8 1TR, United Kingdom

^{a)} Author to whom correspondence should be addressed: alper.celik@bristol.ac.uk

^{b)} Electronic mail: yannick.mayer@bristol.ac.uk

^{c)} Electronic mail: m.azarpeyvand@bristol.ac.uk

ABSTRACT

This paper presents an experimental study on the aeroacoustics of a flat plate rig with a highly instrumented serrated trailing-edge. The role of near-field flow properties, namely, surface pressure fluctuations and spanwise coherence, in the noise suppression capability of serration is not properly understood. The results from this test rig aim to provide additional insight into the effects of the serration on the hydrodynamic field (flow field) and the scattering of the pressure waves along the trailing-edge. Despite its unconventional size, beamforming results showed a significant reduction of far-field noise over a broadband frequency range. The associated flow field is characterized by mean and spectral analyses of static and dynamic surface pressure measurements as well as hot-wire measurements. The mean pressure coefficient results and the boundary layer velocity profiles over the serrated trailing-edge showed minute differences compared to the baseline straight trailing-edge. However, the frequency-dependent energy content of the unsteady surface pressure fluctuations demonstrates an elevated energy region around the serration edges at low frequencies. Although there is an increase in the energy content of the low frequency pressure fluctuations on the serrated trailing-edge, a significant phase difference of the pressure waves is observed, which may be indicative of destructive interference. The temporal studies regarding the unsteady surface pressure fluctuations corroborate the presence of quasi-periodic large scale structures emanating from the serration edges.

© 2021 Author(s). All article content, except where otherwise noted, is licensed under a Creative Commons Attribution (CC BY) license (<http://creativecommons.org/licenses/by/4.0/>). <https://doi.org/10.1063/5.0054767>

I. INTRODUCTION

The broadband noise radiated from airfoils has become an important research topic due to its ubiquitous presence in daily life in the last few decades. The prevalence of wind turbines and the rapid increase in air transport within the last decades have raised environmental noise features as one of the main concerns related to physical and mental health organization (WHO).¹ Due to challenging limitations imposed by stringent noise regulations (e.g., ACARE Flightpath 2050²) and the necessity to further improve the efficiency of wind turbines by increasing power production while reducing cost per unit of generated electrical energy,³ attenuation of the noise emerged as a critical goal.

Out of the five airfoil self-noise mechanisms reported in Brooks *et al.*,⁴ the noise generated by the interaction of convected eddies within a boundary layer with a sharp trailing-edge is identified as the main contributor of the airfoil self-noise. The theoretical works to understand the mechanisms behind the trailing-edge noise radiation for a straight trailing-edge have been categorized by Howe⁵ into three categories: those based on the Lighthill's acoustic analogy, e.g., that of

Williams *et al.*,⁶ linearized hydroacoustic methods, and, e.g., those of Amiet,^{7,8} Chase,⁹ and *ad hoc* approaches. Each one of these three methods requires information about the flow domain, either the turbulent velocity field (two-point correlations) or the unsteady surface pressure fluctuations near the edge. The endeavor to explore the theory and corresponding physics of the noise generation mechanism also helped scientists and engineers to develop noise attenuation devices to reduce and manipulate the noise generated by the bodies immersed in flow, such as aircrafts, wings, and wind-turbines. Noise attenuation methods involve both active and passive ways. Active ways, which require additional energy input to the noise reduction system, involve perturbation of the boundary layer by flow injection,¹⁰ suction,¹¹ and plasma actuators.¹² Due to easier implementation, research on passive noise methods attracted more attention during the last decade. Employing porous materials,^{13–18} changing the trailing-edge geometry,^{19–26} and employing add-on devices such as riblets²⁷ are the most common methods researchers focused on.

Serrations, a type of trailing-edge geometry modification and the subject of this work, have been identified as one of the most efficient ways of reducing noise and were analytically analyzed by Howe.¹⁹ Howe's theory suggests that the noise reduction is a function of effective span-wise length for a sawtooth serrated trailing-edge, which also depends on geometric parameters such as serration length ($2h$) and wavelength (λ). Moreover, in this work it was shown that the noise reduction is strongly dependent on the frequency, and the serrations do not affect the noise generated by large eddies (large wavelength). The model Howe developed predicts an asymptotic reduction of $10\log_{10}[1 + (4h/\lambda)^2]$ for high frequencies. In their works, Howe¹⁹ and Gruber *et al.*²⁸ discussed the recommended practice of employing trailing-edge serrations. To achieve noise reduction, the boundary layer thickness should be in the same order of the serration length, and the serration angle should be narrow ($\varphi < 45^\circ$). Following Howe's work, an extensive amount of research has been conducted on serrations involving experimental,^{20,21,28–31} numerical,^{32–34} and semi-analytical work^{35,36} to understand the underlying physical mechanism and improve the noise attenuation capability. However, recent experimental studies reveal a discrepancy between the predicted results and measured noise reduction levels. These discrepancies^{28,37,38} can be due to the frozen turbulence assumption or the choice of the Green's function as addressed in Avallone *et al.*²⁰

The inadequacy of theoretical models and lack of fundamental knowledge on the underlying mechanisms of noise reduction performance of serrations prevent further improvements in serration designs and their deployment. For the latter, the literature addresses two major mechanisms responsible for noise reduction. The first mechanism is the changes to the flow field (hydrodynamic field) due to the presence of the serration, which is addressed by several recent works.^{20,21,29,32} Chong and Vathylakis²¹ showed that the wall-pressure spectral density and the span-wise coherence values do not contribute significantly to noise reduction. Their work has shown the presence of the pressure-driven vortical structures along the edge of the serrations on flat plate may contribute to any noise reduction. Following this study, Avallone *et al.*²⁰ showed the presence of these side-edge vortices via time-resolved particle image velocimetry measurements over a serrated NACA0018 airfoil. The generation of counter-rotating edge vortices is reasoned by the pressure difference between the suction side and pressure side of the wing.³³ However, for one-sided flat plate experiments, this condition does not exist, yet the foot-print of vortical structures is evident.²¹ Moreover, these observations disprove the validity of the frozen turbulence assumption, which is employed in analytical models for predicting noise reduction. The second possible noise reduction mechanism is identified as the destructive interference generated by pressure waves scattered at different phases, as addressed by Howe¹⁹ and Avallone *et al.*³⁰ Moreover, to improve the noise reduction prediction Lyu *et al.*³⁵ proposed a semi-analytical model based on the noise prediction through surface pressure fluctuations. In this model, the non-dimensional parameters $k_1 \times 2h$, where k_1 is the acoustic wave-number in the stream-wise direction, and l_z/λ was identified as the major parameter of noise reduction. This method was implemented by Mayer *et al.*³⁶ and validated for realistic airfoils. This model suggests that the serrations are effective if only the serration length is long enough to generate phase difference among the pressure waves scattered at the edges. In their recent numerical work, Avallone *et al.*³⁰ provided evidence to support this theory and concluded that the

destructive interference between scattered acoustic pressure waves is the main contributor for noise reduction. Although many new variations of the serrations are proposed,^{39–42} the lack of consensus regarding the underlying mechanisms of the serrations ability to reduce noise requires further attention and research to enable more advanced engineering designs.

The complexity of comparing studies in the literature and understanding the physical phenomena behind the noise reduction arises due to the broad range of the geometries and flow conditions explored in the literature. Studies cover airfoils with serration add-ons,^{32,38,42} airfoils with serration cut-ins,⁴³ flat plates under one-sided flow,²¹ and flat plates under two-sided flow,²⁹ as well as studies at different angles of attack and different serration lengths and wavelengths, which prevents a comprehensive understanding of the physical mechanism of noise reduction. Although the flow conditions are well documented in the literature, each study investigates different parameters, and not all experiments are reporting the same quantities, which may lead to a lack of grasping the physics and understanding the mechanism behind the noise reduction. However, it is of utmost importance to understand each physical mechanism's contributions to improve the design of serrations and understand the limits of the design space.

This paper presents the results of an experimental study of a serrated flat plate under one-sided flow to contribute to the understanding of the noise reduction mechanism of serrated trailing-edges and to provide evidence for noise reduction of large scale serrations ($2h \approx 92$ mm, $\lambda \approx 116$ mm in width, $\delta/2h = 0.16$, and $\lambda/2h = 1.25$) in conjunction with the associated flow field. This design may overcome the addressed issues⁴⁴ on robustness for current designs, as it is not fragile and can be installed easily. This paper is structured as follows: Sec. II presents the experimental methodology, the anechoic wind tunnel, and the measurement methods. Section III presents the results of the experiments. The results include beamforming measurement results, unsteady and steady pressure measurement results, and velocity field measurement results on the serration. Finally, Sec. IV concludes the discussion.

II. EXPERIMENTAL METHODOLOGY

In this section, the details of the experimental facility, the instrumentation of the experimental rig, and the measurement techniques are provided.

A. Anechoic wind tunnel facility and serrated flat plate

Experiments were performed in a closed-circuit open-jet anechoic wind tunnel facility at the University of Bristol. The wind tunnel has a stable performance for velocities of up to 40 m/s with turbulence levels as low as 0.2%.⁴⁵ The nozzle of the wind tunnel is 775 mm in height and 500 mm in width with a flow uniformity over 90% at the nozzle exit. The preliminary experiment results showed that the flow field and far-field characteristics were observed to be independent of the Reynolds number for the free-stream velocities of $10 \text{ m/s} < U_\infty < 30 \text{ m/s}$. Therefore, for brevity, all results are presented for a free-stream velocity of $U_\infty = 20 \text{ m/s}$, which yields a plate length based Reynolds number of $Re_L \approx 8 \times 10^5$. The flow was tripped via a zig-zag turbulator strip at 10% of the flat plate length to ensure the presence of a fully turbulent boundary layer over the flat plate and trailing-edge.

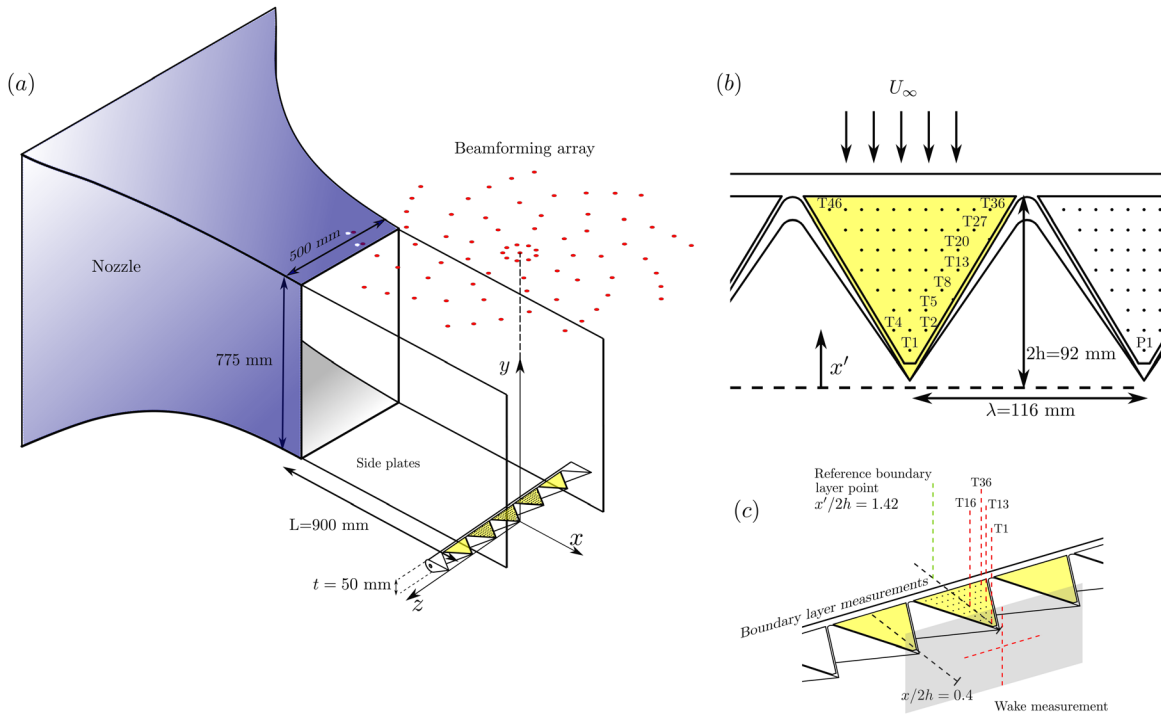


FIG. 1. Details of the experimental rig, (a) schematics of the test rig and serrated flat plate, (b) details of the serration geometry, and (c) hot-wire measurement locations.

The flat plate has a length of $L = 900$ mm and was mounted at the bottom lip of the nozzle. The flow was bound by the side plates on either side, which were 250 mm longer than the flat plate. The schematics of the test rig including the details of the serration and hot-wire measurement planes are presented in Fig. 1. The trailing-edge of the flat plate is designed to have a serration length ($2h$) of 92 mm and a wavelength (λ) of 116 mm, resulting in a serration angle of $\varphi \approx 50^\circ$. The serration has a thickness of 50 mm at its root. It is worth noting that the experiments were conducted under one-sided flow; hence, the thickness at the root is not assumed to have a significant effect in terms of vortex shedding. The serration can be modified into a straight trailing-edge flat plate by utilizing 3D printed fillers to obtain results for a baseline case. The serrated flat plate rig was instrumented heavily

to explore the flow field generated over the serration. Figure 1(b) provides an illustration of the distribution of the unsteady pressure transducers (T) and the steady pressure measurement taps (P), with a total of 46 unsteady pressure transducers, and 46 steady pressure taps were employed during the measurements. A global coordinate system (x, y, z) was defined with its origin located at the trailing-edge on the symmetry axis of the test rig in order to define global scalar and vector fields as well as the test rig location. A local coordinate system (x', y') is designated to ease the interpretation of the results. x' is defined as the upstream distance from the trailing-edge. The local wall-normal distance y' represents the distance from the surface for a designated x' location and was employed for the discussions of the boundary layer measurements. The locations of the transducers are provided in Table I.

TABLE I. Locations of the unsteady surface pressure transducers and steady pressure taps with respect to the local coordinate system.

Transducer	$x'/2h$	$z/2h$	Pressure tap	$x'/2h$	$z/2h$
T1	0.15	0	P1	0.15	-1.26
T2, T3, T4	0.26	-0.08, 0, 0.08	P2, P3, P4	0.2	-1.18, 0, -1.34
T5, T6, T7	0.37	-0.08, 0, 0.08	P5, P6, P7	0.37	-1.18, 0, -1.34
T8,...,T12	0.48	-0.16,...,0.16	P8,...,P12	0.48	-1.10,..., -1.42
T13,...,T19	0.59	-0.24,...,0.24	P13,...,P19	0.59	-1.02,..., -1.50
T20,...,T26	0.70	-0.24,...,0.24	P20,...,P26	0.70	-1.02,..., -1.50
T27,...,T35	0.81	-0.32,...,0.32	P27,...,P35	0.81	-0.94,..., -1.58
T36,...,T46	0.92	-0.40,...,0.40	P36,...,P46	0.92	-0.86,..., -1.66

B. Acoustic beamformer

The far-field measurements were performed with an in-house built beamforming array. The center of the beamforming array was positioned 1.2 m directly above the trailing-edge of the flat plate, as illustrated in Fig. 1. The 73 Panasonic WM-61A microphone array consists a central microphone and nine spiral arms with eight microphones each, spanning a circular region with a diameter of 0.8 m. The beamforming measurements were performed for 120 s at a sampling frequency of 2^{15} Hz. The measurements were then post-processed using the open-source Acoular Beamforming package⁴⁶ to obtain functional beamforming maps for frequencies of $600 < f < 3200$ Hz. The beamforming analysis is performed with a spatial resolution of 0.01 m. The cross power spectral density matrix was calculated with a Hanning window, a block size of 4096, and an overlap of 50%. The measurement uncertainty of the Panasonic microphones was calculated to be 1.5 dB for a 95% confidence interval.

C. Unsteady and steady surface pressure measurements

The steady pressure measurements were conducted using two 32-channel Chell MicroDaq Smart Pressure Scanners. The steady pressure data were collected for 16 s, with a sampling frequency of 1000 Hz. The propagated uncertainty value was 2.5% for the lowest measured pressure values. The unsteady pressure measurements on the flat plate were carried out using the *in situ* microphone instrumentation, allowing for a detailed evaluation of the near-field pressure fluctuations. A total number of 46 Knowles FG-23329-P07 miniature pressure transducers were used for this purpose. The microphones are 2.6 mm in diameter and have a sensing diameter of 0.8 mm. The rig was machined to have a pinhole mask over the microphones with a diameter of 0.4 mm to avoid pressure attenuation at high frequencies.⁴⁷ All microphones were calibrated in phase and magnitude with a GRAS 40PL reference microphone, which was calibrated using a GRAS 42AA pistonphone calibrator. The data were acquired using National Instrument PXIe-4499 module and were sampled at 2^{16} Hz for a duration of 16 s. The microphone locations are presented in Table I. The surface pressure data obtained give an absolute uncertainty of 0.05%dB with a 95% of confidence level.

D. Hot-wire anemometry

The mean velocity field and turbulent characteristics of the flow field were obtained by hot-wire measurements on the trailing-edge. Boundary layer velocity measurements over the trailing-edge were performed using a Dantec 55P15 boundary layer probe. The probes were operated by a Dantec Streamline Pro system with a CTA91C10 module with a low-pass filter with a cutoff frequency of 30 kHz. The measurements were performed at a fixed overheat ratio of 0.8 for all measurements. Each probe was calibrated using a Dantec 54H10 calibrator, while the cross-wire probes were also calibrated between the yaw angles of -40° and 40° . All hot-wire measurements were simultaneously sampled with the microphone measurements at a frequency of 2^{15} Hz for 60 s using the National Instruments PXIe-4499 modules mounted in a National Instruments PXIe-1062Q chassis. Hot-wire probes were traversed using a two-axis ThorLabs LTS300M system. The boundary layer measurements were conducted at 40 wall-normal locations on top of the pressure transducers T1, T13, T16, and T36 and an additional upstream location before the serration as reference at $x'/2h = 1.42$ and $z/2h = 0$. The total distance for 40 stations covers 140 mm, which is well above the boundary layer thickness, and ensures that the change in the velocity is below 0.5% between consecutive stations.

III. RESULTS AND DISCUSSION

A. Far-field measurements

In this section, the far-field noise is presented to confirm the validity of using a non-conventional serration of $h/\delta = 3.1$ and $h/\lambda = 0.4$, by providing evidence that it achieves far-field noise attenuation when compared to a straight trailing-edge flat plate. Figure 2 presents beamforming source maps at frequencies of $f = 600, 1500,$ and 2500 Hz. The contour maps provide the difference of the sound pressure levels between the serrated trailing-edge (SER) and the straight trailing-edge (STR), defined as $\Delta SPL = SPL_{SER} - SPL_{STR}$. Hence, a negative value denotes a noise reduction due to presence of serrated trailing-edge. The individual source maps of the SER and STR cases are not presented for brevity. A schematic of the serrated flat plate is also included in the figure to ease the interpretation of the results. The results indicate that the primary noise source is located around the trailing-edge, and the serrated trailing-edge attenuates the noise over a broad range of frequencies. The employed serration

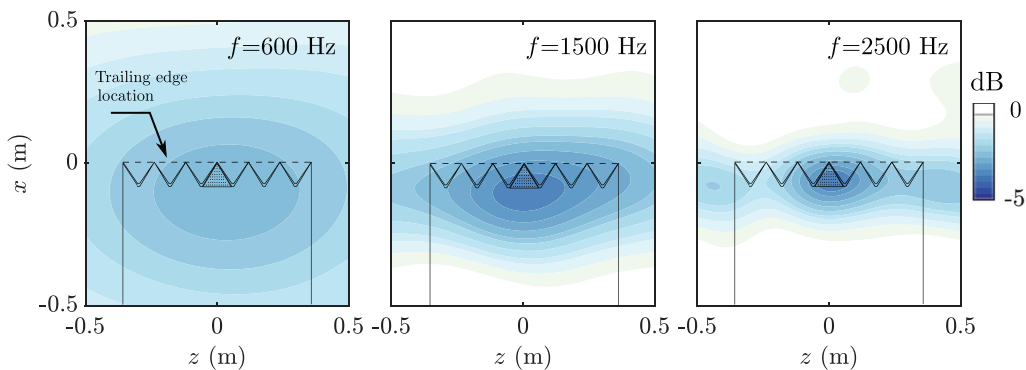


FIG. 2. Beamforming source maps for $\Delta SPL = SPL_{SER} - SPL_{STR}$ at (a) $f = 600$, (b) 1500, and (c) 2500 Hz.

achieves a noise reduction between 2 and 4 dB over the measured frequency range.

Figure 3 is presented to provide more information about the noise reduction performance across the measurement spectra. The presented SPL values are averaged over a rectangular grid of $-0.1 < x < 0.1$ and $-0.15 < z < 0.15$ m. Although the source power integration (SPI) is a powerful technique to obtain SPL values with better accuracy,⁴⁸ the comparative nature of this study allows discussions based on simple averaging. It is worth noting that the low frequency and high frequency limits of the beamforming is dictated by the point spread function and the spatial resolution of microphone array, respectively. The SPL results suggest that the serrated flat plate consistently radiated less noise compared to the straight trailing-edge baseline case. The noise reduction is most significant at around $f=1500$ Hz. Moreover, at low and high frequencies, the noise reduction performance deteriorates, as previously observed by Chong and Vathylakis.²¹

Howe⁴⁹ analytically showed that serrations with a wavelength of λ and a root-to-tip distance of $2h$ could achieve more than $10 \log_{10}[1 + (4h/\lambda)^2]$ dB noise reduction compared with the straight trailing-edge counterpart. For the current configuration in this study, Howe's formula suggests a 5.5 dB reduction, which is relatively close to the observed noise reduction level. Although the reduction levels are slightly lower than the predicted results obtained through the analytical model provided by Howe,^{19,49} it is consistent with the results provided by the recent experimental works of Gruber *et al.*,³¹ Moreau and Doolan,²⁹ Fischer *et al.*,⁵⁰ and Zhou *et al.*,⁵¹ where the achieved noise reduction is less than predicted. Howe's theory suggests that serrations achieve efficient noise reductions for $\omega\delta/U_c > 1$, where ω stands for the angular frequency ($2\pi f$) and U_c stands for the convection velocity. In their work, Gruber *et al.*²⁸ reported noise reductions up to $\omega\delta/U_c \approx 9$. Interestingly, in this study, the noise reduction is achieved for a broad range of frequencies over $3.9 < \omega\delta/U_c < 16.3$. A further comparison with Howe's theory can be built around the non-dimensional parameters h/λ and h/δ . For the noise reduction mechanism, Howe's theory suggests that scattered pressure waves generate a constructive-destructive interference for $h/\delta \approx 1$, which generates an oscillatory far-field noise spectrum. However, recent studies reveal that

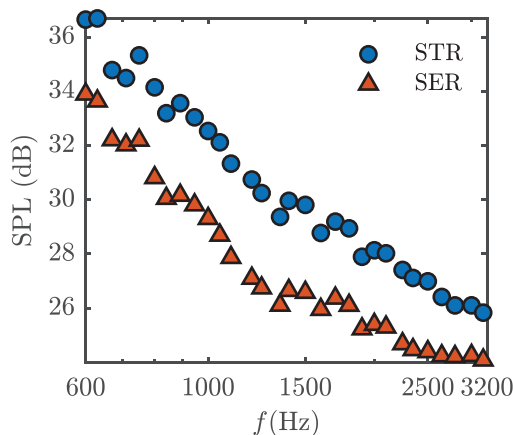


FIG. 3. Comparison of averaged sound pressure values for STR and SER cases for frequencies of $600 < f < 3200$ Hz.

the constructive-destructive interference play an important role in the noise reduction mechanism.^{30,35} Moreover, the predicted oscillatory far-field behavior due to the interference at $h/\delta \approx 1$ was not observed in experimental measurements.³¹ Finally, considering the effect of h/λ , Howe's theory suggest prominent noise reduction with an increase in h/λ due to skewed angle of incidence of turbulence structures with the edge. For the current study $h/\lambda = 3.1$ and a maximum noise reduction of around 4 dB is achieved.

These results and discussions underline the inadequacy of the aforementioned theories and reasoning for the noise reduction mechanisms of the serrations. The analytical models of Howe¹⁹ and Lyu *et al.*³⁵ are derived based on the scattering mechanism and hence neglect any changes in the flow field (hydrodynamic field). Moreover, the frozen turbulence assumption employed in the derivation of the analytical models has been shown to be not fully accurate by a number of studies.^{20,29,31} Sections III B–III E will focus on the steady and unsteady characteristics of the flow field over the serrated flat plate to shed light on the possible noise reduction mechanisms for this current configuration and understand the relation between geometric parameters, flow quantities, and far-field noise in relation to the literature.

B. Time-averaged flow field

The mean flow field over the serrated flat plate is characterized by presenting time-averaged (mean) velocity profiles, root mean square (rms) velocity profiles, probability density functions of pressure signals (PDF), dimensionless mean-pressure coefficients (C_p), rms mean-pressure coefficients ($C_{p,rms}$), and time-histories of pressure (p') and rms pressure (p'_{rms}) values.

Figure 4 presents the effect of the serrated trailing-edge on the velocity profiles and rms velocity values at transducer location T1, i.e., $x'/2h = 0.15$ and $z/2h = 0$, in comparison to the results from the straight trailing-edge. Both the velocity and the rms velocity profile show that the presence of the serration does not alter the mean quantities at the trailing-edge. This observation is consistent with Jones and Sandberg,³² and León *et al.*³⁸ The reference boundary layer thickness, δ_o , was measured at an upstream location ($x'/2h = 1.42$ and $z/2h = 0$) and was $\delta_o = 14.5$ mm. Moreover, it is worth noting that the boundary layer thickness and corresponding u'_{rms} profile do not show a significant change at the T1 location ($x'/2h = 0.15$ and $z/2h = 0$) when compared to the upstream measurement results.

Although the time-averaged (mean) velocity data are not affected by the presence of the serrations, the time-history plots of the pressure data reveal a marked change in the pressure field. Figure 5(a) shows the time-history of the pressure obtained through pressure transducers T1 ($x'/2h = 0.15$ and $z/2h = 0$) and T16 ($x'/2h = 0.59$ and $z/2h = 0$) for both the serrated trailing-edge (SER) and the baseline straight trailing-edge (STR). The time-history results in Fig. 5(a) demonstrate that the presence of the serration introduces large scale oscillations in the pressure field at the T1 location ($x'/2h = 0.15$), an effect which is less pronounced at the T16 location ($x'/2h = 0.59$ and $z/2h = 0$). Additionally, $\pm p_{rms}$ values for both cases at the T1 location are also displayed on the plots. The results indicate that the serrated trailing-edge increases the rms fluctuations of pressure compared to the STR case. However, the serrated case displays no significant extreme pressure events (events beyond rms boundaries), contrary to results reported by Chong and Vathylakis.²¹ Further insight into the pressure signals can be obtained through probability density functions

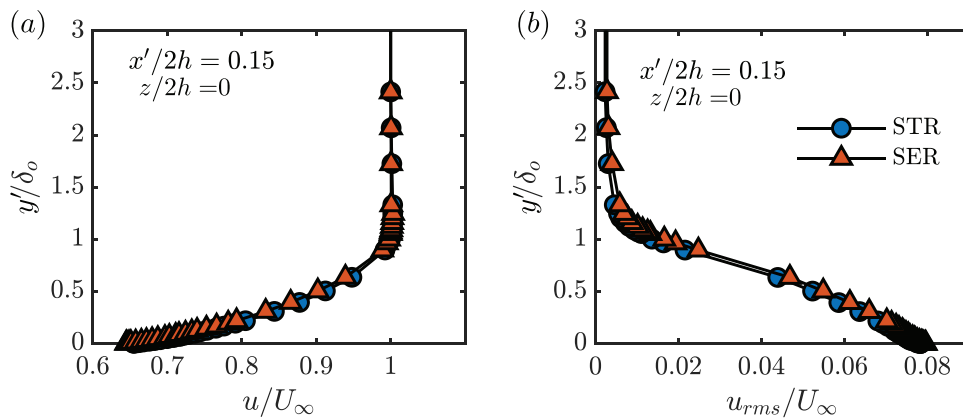


FIG. 4. Comparison of (a) time-averaged (a) velocity profile and (b) rms velocity profile at stream-wise location $x'/2h = 0.15$ and $z/2h = 0$, over transducer T1.

(PDF). The PDF of the pressure fluctuations are presented for the STR and SER cases at T1 and T16 in Fig. 5(b). The fluctuation values were normalized by the standard deviation for each pressure level for each case. A normalized Gaussian distribution is presented as a reference. It is worth noting that any deviations from the Gaussian distribution indicate that the flow is dominated by characteristic pressure events.⁵² At T16, the PDF distribution of pressure data for both the STR and SER cases has similar trends, which is consistent with the time-history results presented in Fig. 5(a), showing that the presence of the serration is not affecting the upstream location T16. At the trailing-edge, T1, the distribution of the surface pressure PDFs exhibits quasi-exponential tails deviating from Gaussian distribution for the STR case, whereas for the SER case, the PDF exhibits a quasi-Gaussian trend. These results clearly indicate that the pressure events significantly differ at the T1 location between the STR and SER case. The figure also presents the effect of the serration on the mean (C_p) and rms ($C_{p,rms}$) pressure coefficient in terms of the change in the magnitude, i.e., $\Delta(\cdot) = (\cdot)_{SER} - (\cdot)_{STR}$. For brevity, the results of the C_p and $C_{p,rms}$ are presented on the each respective half of the geometry. C_p and $C_{p,rms}$ values were calculated using the data obtained from steady pressure transducers (P1–P46). The extremely low values of ΔC_p results indicate that the presence of the serration does not have a significant effect on the mean static pressure. However, a notable change is evident in the $\Delta C_{p,rms}$ results. The $C_{p,rms}$ values are elevated markedly along the serration edge. This increase may be due to the generation of vortical structures along the edges of the serration, as addressed by Avallone *et al.*²⁰ as well as Chong and Vathylakis.²¹ This observation will be detailed further through the analysis of the unsteady surface pressure fluctuations.

C. Unsteady surface pressure fluctuations

In Sec. III B, the main focus was to highlight the effect of the presence of the serration on the mean flow field. In this section, a detailed analysis of the frequency-dependent energy content of the unsteady surface pressure fluctuations will be presented to further comprehend the effect the serration has on the flow field and radiated noise. In his classical work, Amiet⁸ stipulates a proportionality between the unsteady surface pressure spectra (S_{qq}) and radiated far-field noise (S_{pp}). Moreover, the span-wise correlation length (Λ_p), which is also a function of unsteady surface pressure spectra, is also addressed as

a major contributor to the radiated far-field noise in Amiet's model. The spanwise length-scale of the coherent structures (correlation length) is further underlined as an important parameter by Howe¹⁹ and Lyu *et al.*³⁵ to understand the noise reduction mechanism of serrations, which can be calculated through coherence analysis. This section will be devoted to present quantities that can be deduced from surface pressure spectra and to further explore the effect of the serration geometry on the flow field and their effect on the radiated far-field noise.

Figure 6 presents the power spectral density of the surface pressure fluctuations (PSD) obtained from the pressure transducers along the centerline of the serration (T1, T3, T6, T10, and T41) and along the edge of the serration (T1, T2, T5, T13, and T36), in comparison with the results obtained from transducers along the centerline of the baseline straight trailing-edge. The spectra of the unsteady surface pressure fluctuations are obtained by employing Welch's method⁵³ using a Hamming window for equal length segments with 50% overlap, resulting in a frequency resolution of 2 Hz. An illustration of the test cases with color coded transducer locations is provided to ease the results' interpretation. The PSD results for the straight trailing-edge case, Fig. 6(a), show a gradual increase toward the trailing-edge. At mid-frequencies, the PSD results scale with f^{-1} as expected. At higher frequencies, above $f = 3000$ Hz, the PSD scales with f^{-5} . These observations are consistent with the literature.⁵⁴ Figure 6(b) exhibits how the serration affects the surface pressure fluctuation spectra along the centerline of the rig. At low frequencies, a broadband energy increase builds toward trailing-edge, where it peaks at the apex of the serration (T1). This broadband hump centers around $f = 150$ Hz and broadens toward the trailing-edge. At higher frequencies, the surface pressure fluctuations follow a similar trend to that of the baseline STR case, except for the furthest upstream location. Further observations can be deduced from the PSD results obtained along the serration edge, as displayed in Fig. 6(c). The broadband energy increase at low frequencies is similar at the apex, but more prominent at the upstream measurement locations. The PSD results are significantly higher for the transducers along the edge (T2, T5, and T13) when compared to the results from the transducers situated on the centerline of the serration at the same stream-wise location (T3, T8, and T16). These results corroborate the presence of energetic structures along the edge of the serrations.

The spatial extent of these elevated energy regions is explored further in the contour plots of Fig. 7, displaying the change in the

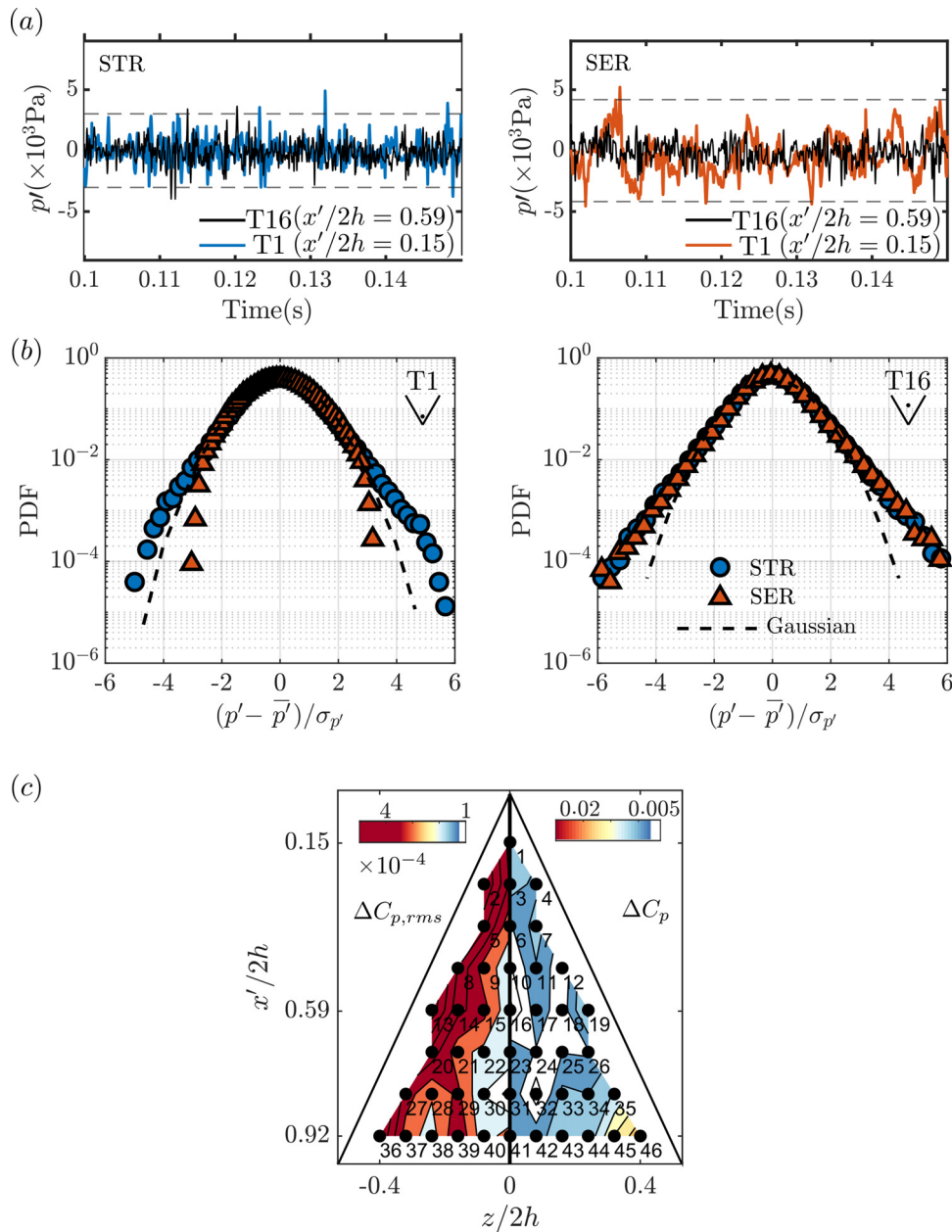


FIG. 5. (a) Comparison of the time-history of the pressure data for STR and SER cases at T1 ($x'/2h = 0.15$) and T16 ($x'/2h = 0.59$), rms pressure value at T1 is displayed as $\pm p_{rms}$ (dashed line), (b) PDF of pressure signal at T1 and T16 for STR and SER cases, and (c) contours of $\Delta(\) = (\)_{SER} - (\)_{STR}$ for C_p and $C_{p,rms}$.

power spectral density of surface pressure fluctuations in the case of serrated trailing-edge ($\Delta PSD = PSD_{SER} - PSD_{STR}$). The results are presented for two selected frequencies representing the low-frequency phenomena observed at around $f = 150$ Hz and the typical behavior at mid-to-high frequencies at around $f = 1500$ Hz. Considering Fig. 7(a), the results show that an increase in the low-frequency energy content builds up toward the serration edges for the serrated trailing-edge case. This build-up from two edges amalgamates at the trailing-edge, i.e.,

the apex of the serration, where a significantly increased energy level is present. This observation is consistent with the observations in Avallone *et al.*²⁰ and Chong and Vathylakis.²¹ At $f = 1500$ Hz, the near-zero results exhibit an insignificant change in the level of the energy content over the serration region compared to the straight trailing-edge case (STR). These results indicate that the surface pressure spectra show a significant increase on the serrations' edges only at low frequencies. Since the elevated regions do not emerge at the root

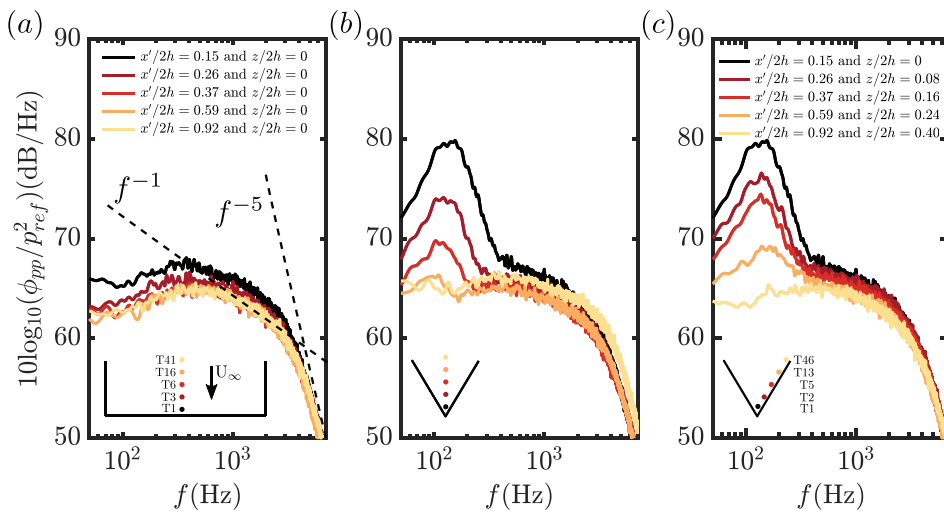


FIG. 6. Comparison of the power spectral density of the unsteady surface pressure fluctuations for STR and SER cases along (a) the centerline of the straight trailing-edge, (b) the centerline of the serrated trailing-edge, and (c) along the edge of the serration. ($p_{ref} = 2 \times 10^{-5}$ Pa and denotes the reference pressure.)

of the serration, it may be assumed that the elevated regions are not due to bluntness shedding. However, the shedding may be due to the development of vortical structures along the serration edges, as observed in previous studies in the literature.^{20,21,33} Considering these results in conjunction with the Amiet’s theory, the far-field results should show an increase at low frequencies due to the increase in the energy of the surface pressure spectra. However, due to the limitations of the beamforming array, measurements could not be extended to low frequencies. At mid-frequencies, $f = 1500$ Hz, the unsteady surface pressure spectra suggest no significant change. Yet, the far-field results show a significant reduction of noise levels for these frequencies.

In order to further investigate the presence of the elevated energy regions around the edges of the serration at low frequencies, phase maps over the serrated region are calculated with respect to transducer T1. The phase difference is calculated through estimating the cross-spectrum of pressure signal between T1 and rest of the transducers. Figure 8 presents the contours of the phase differences with respect to T1 over the serration at $f = 150$ Hz for both the STR and SER cases. Considering the results for the STR case, a well-defined phase change pattern is evident from upstream toward downstream. A complete cycle of the phase from $-\pi$ to π is observed over roughly the size of the

serration, which clearly indicates that the dominant feature in the pressure data is associated with the hydrodynamic field. More importantly, the phase difference map for the SER case reveals a notably different map. The phase results indicate a significant deviation from a typical cyclic behavior of an undisturbed wave pattern, as in STR case. The center of the serration is dominated by a positive phase difference, gradually evolving toward the reference transducer T1. However, along the edges of the serration, the presence of symmetric isolated opposite phase islands suggests a fundamental change in the hydrodynamic field over the serration compared to the STR case. It is worth noting that even for a highly instrumented test rig, the hydrodynamic pressure pattern on the baseline case can be only captured for low frequencies by eight transducers. The root-to-tip distance of the serration is approximately 0.1 m, which allows capturing the hydrodynamic wave propagation at very low frequencies ($U/f \approx 0.1$ m). However, for higher frequencies, where far-field noise measurements can be performed, the hydrodynamic wavelength reduces to the order of a few centimeters or less. Therefore, capturing the wave patterns and the phase difference along the serration becomes extremely challenging considering the state-of-the-art experimental capabilities.

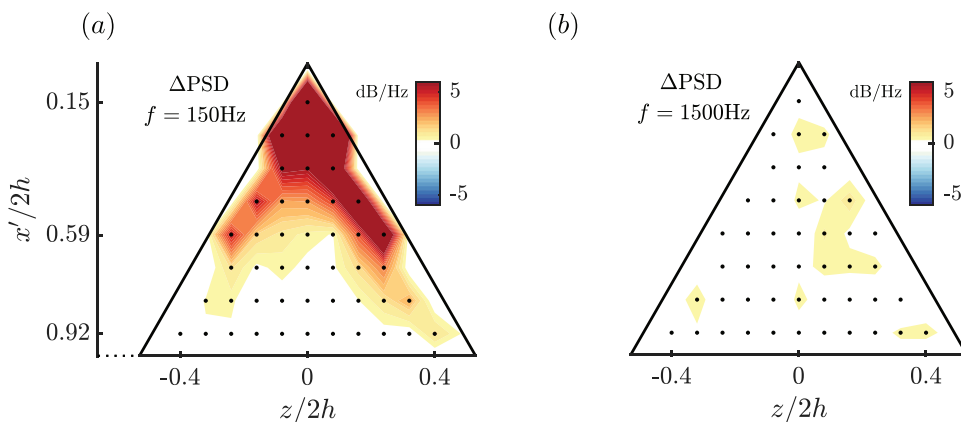


FIG. 7. Contours of ΔPSD ($PSD_{SER} - PSD_{STR}$) over the trailing-edge (a) $f = 150$ and (b) $f = 1500$ Hz.

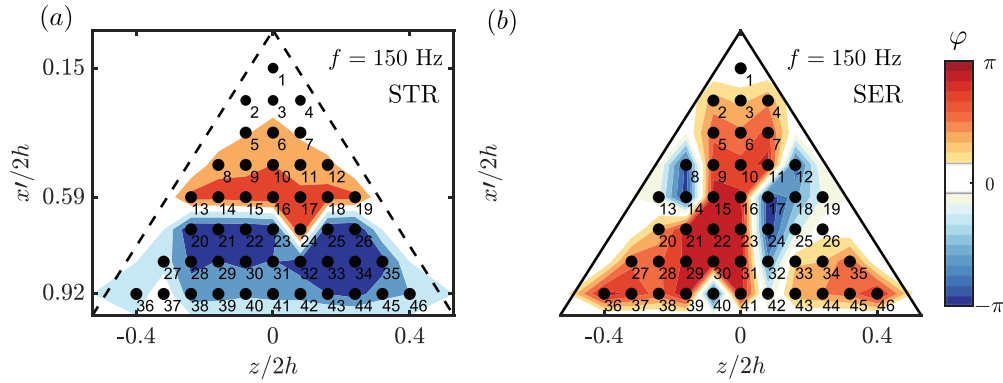


FIG. 8. Contours of phase differences in radians with respect to transducer T1 over the serrated region at $f = 150$ Hz for (a) STR case and (b) SER case.

The stream-wise and span-wise (lateral) coherence of the surface pressure fluctuations is also evaluated to corroborate the results provided by the spectra of the surface pressure fluctuations. Through the coherence studies, the foot-print of the development of the flow structures may be observed. The magnitude-squared stream-wise (or span-wise) coherence is calculated as

$$\gamma_{p_i p_j}^2(f, \xi) = \frac{|\phi_{p_i p_j}(f)|^2}{|\phi_{p_i p_i}(f)| |\phi_{p_j p_j}(f)|}, \quad (1)$$

where $\gamma_{p_i p_j}^2(f, \xi)$ denotes the magnitude-squared coherence calculated between two transducers located at two different locations and separated by a distance of ξ and $\phi_{p_i p_j}$ denotes the cross-power spectral density between those transducers. Physically, the coherence function provides an indication of the relation between measured quantities at two separate locations and allows elucidating the connection between them.

For a detailed study, the coherence of the signals obtained from the transducers at the centerline and along the edge of the serration is calculated with respect to the transducer T1 ($x'/2h = 0$ and $z'/2h = 0$) and presented in Fig. 9. The coherence magnitudes are plotted against frequencies up to 2000 Hz, beyond where the values become indiscernible. Figures 9(a) and 9(b) show the coherence values of signals at transducers T3, T6, T10, T16, and T23 with respect to T1 for straight and serrated trailing-edge, respectively. Likewise, Figs. 9(c) and 9(d) present the results for the transducers lying on the edge of the serration geometry T2, T5, T8, T13, and T20 (and same transducers for the straight trailing-edge case). The results obtained along the centerline for the straight-trailing-edge case, Fig. 9(a), show a typical boundary layer behavior, where a broadband coherence is observed due to the presence of different sized structures within the boundary layer. The coherence fades out at further upstream measurement locations, as expected. Moreover, there is no significant coherence between the signal from T1 and other transducers located along the line, where the serration edge would lie, for the straight trailing-edge case. Coherence results in Fig. 9(c) indicate that the coherent structures only convect in the stream-wise direction, and the flow is effectively two-dimensional. The coherence results obtained for the serrated trailing-edge case depict a markedly different picture, as shown in Fig. 9(b). The results for this case can be examined in two ways. First, a

significantly elevated coherence is evident at around $f = 150$ Hz, which persists well upstream, indicating a large scale structure over the serration. Second, a broadband coherence exists, which is due to the presence of the turbulent boundary layer. Nonetheless, this broadband behavior is deteriorated and exhibits lower levels of coherence than the STR case results. This region is shaded with a gray color to ease the interpretation. The results indicate that the large scale structures severely affected the fine-scale structures in the boundary layer. Considering the coherence results obtained from transducers along the edge of the serration, Fig. 9(d), it is worthwhile to mention the presence of high levels of coherence at around $f = 150$ Hz. Moreover, above $f = 300$ Hz, no discernible coherence exists. This observation indicates the lack of a boundary layer along the edge, which is expected. More importantly, it also accentuates the existence of large scale structures along the edge of the serration.

Another important parameter that can be evaluated through the integration of span-wise coherence is the span-wise integral length scale (Λ_p) of the eddies convected over the trailing-edge. The integral length-scale of the eddies is a direct contributor to the far-field noise radiation and is utilized in the Amiet's trailing-edge far-field noise prediction model.^{8,32} The span-wise integral length scale is calculated as

$$\Lambda_p = \int_0^\infty \gamma_{p_i p_j}(f, \Delta z) d\Delta z, \quad (2)$$

where $\gamma_{p_i p_j}(f, \Delta z)$ represents the span-wise coherence calculated between two transducers located at z_i and z_p , located at span-wise distances of $0 < \Delta z/2h < 2.4$. Here, $\phi_{p_i p_j}$ stands for the cross-power spectral density, and Δz represents the span-wise distance between the two transducers.

Figure 10 shows the effect of the serration on the span-wise correlation length (Λ_p) calculated using Eq. (2) at $x'/2h = 0.59$. For the STR case, the non-dimensional correlation length scale ($\Lambda_p/2h$) is approximately 0.2 at low frequencies and slightly decreases for frequencies above $f = 400$ Hz. However, the results show a significant increase at the low frequencies around $f = 150$ Hz for the SER case. There is no discernible change at higher frequencies between the two cases. Thus, considering the Amiet's model,⁸ the radiated noise should increase at low frequencies due to the increase in length scale. Nevertheless, due to the experiments' limitations in aeroacoustic facilities, the far-field results at such low frequencies can not be measured.

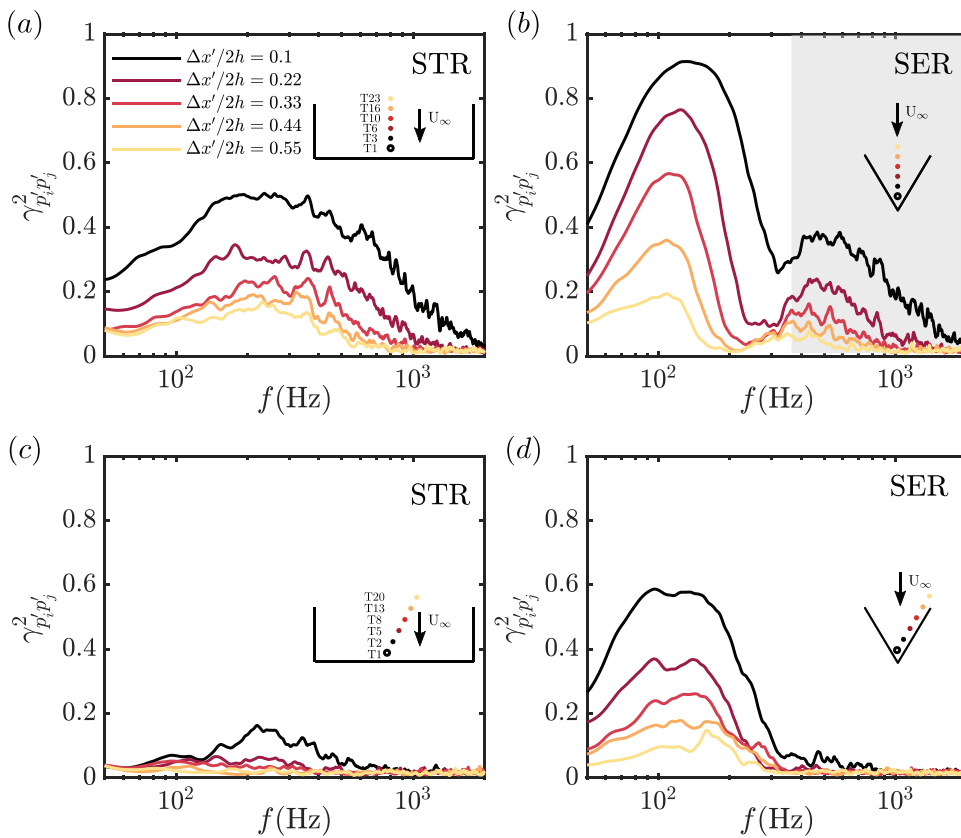


FIG. 9. Magnitude-squared coherence, $\gamma_{p_i p_j}^2(f, \zeta)$, with respect to T1 (a) and (b) along the centerline and (c) and (d) along the edge of the serration for STR and SER cases.

It is worth noting, however, that the far-field noise results in Fig. 3 indicates that the serration does not cause much noise reduction for $f < 400$ Hz. These results are consistent with the recent literature,²⁰ yet underline the inaccuracy of frozen turbulence assumption utilized in analytical models.¹⁹ Another discussion can be built around the constructive-destructive interference theory.^{19,35} These models suggest that the root-to-tip distance of serration should be large enough to allow a phase difference among scattered pressure waves. In addition,

the wavelength of the serration should be smaller compared to the correlation length in span-wise direction to enable interaction of scattered waves to generate destructive interference. The results show that at around $f = 150$ Hz, the coherent structure's length scale is around $\Lambda_p = 40$ mm. At higher frequencies, $f > 1000$ Hz, the length scale is predicted at around $\Lambda_p = 13$ mm and is the same for both STR and SER cases. Recalling the serration dimensions, $2h = 92$ and $\lambda = 116$ mm, and considering the length scale results together with the theories, a phase difference of the scattered pressure waves along the serration edge is expected since $\Lambda_p < 2h$. However, the serration wavelength is larger than Λ_p and does not fulfill the suggestions mentioned in Howe¹⁹ and Lyu *et al.*³⁵ Nonetheless, the far-field results show a significant noise reduction over all the frequency range that can be measured. Finally, it is worth noting that interpreting the integral length scale in comparison to the boundary layer thickness (Λ_p / δ_o) may provide additional insights into the flow field. At frequencies $f > 400$ Hz, the estimated structure sizes are smaller than the boundary layer thickness δ_o , i.e., $\Lambda_p / \delta_o < 1$. However, at lower frequencies, Λ_p is around $2.5\delta_o$, indicating that these structures are not confined to the boundary layer, i.e., indicative of a strong local hydrodynamic field. As such, these larger scale structures may be interpreted as the footprint of three-dimensional vortical structures on the serration.

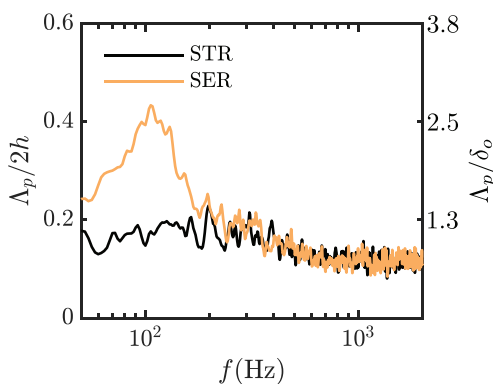


FIG. 10. Estimated span-wise integral length scales at $x'/2h = 0.59$ for transducers located at $0 < \Delta z/2h < 2.4$ with respect to T16 for the SER and STR cases.

D. Temporal analysis of surface pressure fluctuations

Having addressed the spectral characteristics of the surface pressure fluctuations, this section will provide an analysis of the temporal

characteristics of the surface pressure fluctuations. The time scales of coherent structures within the boundary layer help to characterize the turbulent boundary layer and understand the coherent structures present in the flow. To determine the dominant time scales in the flow, an auto-correlation analysis is performed for the unsteady surface pressure fluctuations collected over the flat plate for both the STR and SER cases. The auto-correlation function of the surface pressure fluctuations is defined as

$$R_{p'p'}(x, y, \tau) = \frac{\overline{p'(x, t)p'(x, t + \tau)}}{p_{rms}^2(x, t)}, \quad (3)$$

where p' is the wall pressure signal from the transducer located at x , p_{rms} is the root mean square of the pressure fluctuations p' and τ represents the time-delay between the signals.

Figure 11 is presented to identify and show the dominant time scales in the wall pressure time records. Following the same approach as with the previous figures, the auto-correlation results are presented for the transducers at the centerline of the baseline straight trailing-edge case [Fig. 11(a)], the centerline of the serrated trailing-edge [Fig. 11(b)], and along the edge of the serrated trailing-edge [Fig. 11(c)]. The results are plotted against normalized time delay, $\tau^* = \tau U_\infty / 2h$. For the straight trailing-edge case, the results indicate a fast decay of the $R_{p'p'}$ function for all transducers, exhibiting a typical turbulent boundary layer behavior. For the serrated trailing-edge case, however, the $R_{p'p'}$ functions for both the centerline and edge suggest a more complex physical phenomenon when compared to the STR case. The results for the centerline transducers, Fig. 11(b), suggest the presence of large scale structures, which are evident due to significantly lower decay rates of the $R_{p'p'}$ curves for transducers around the apex of the serration (T1, T3, and T6). Moreover, the sharp change of the auto-correlation to a slower decay rate may be related to the presence of two concurring mechanisms:¹⁴ a quasi-periodic hydrodynamic field with the periodicity (or quasi-periodicity) and a fast-decaying event at around $\tau^* = 0$. Moreover, the negative auto-correlation regions also corroborate the interpretation as the foot-print of regular quasi-periodic large scale structures.⁵⁵ Hence, considering the $R_{p'p'}$ results in conjunction with the coherence results and power spectral density analysis, the presence of edge vortices generated along the edge of the serration becomes more apparent. The results along the edge of the

serration, presented in Fig. 11(c), exhibit similar trends to the results from the transducers along the centerline. However, it is nevertheless worth noting the slight differences from the centerline results. The results from transducers which lie on the same stream-wise distance at the centerline and the edge of the serration, i.e., T2-T3, T5-T6, T13-T10, and T36-T41, highlight two important differences. First, the large scale motion is felt more strongly at the edge of the serration at T3 compared to the T2 and is evident due to a higher correlation magnitude. Moreover, at location T3 on the centerline, the kink on the $R_{p'p'}$ curve is smoother than its counterpart on the serration edge, T2. Second, further upstream, the large scale quasi-periodic event is evident in the autocorrelation function for location T13 with a sudden expansion. However, for the same stream-wise distance at T10, the $R_{p'p'}$ curve exhibits a typical boundary layer behavior without any indication of a secondary event. These observations corroborate the generation of vortical structures at the edges of the serration.

To further understand the effect of serration on the flow field and to elucidate the behavior of the vortical structures generated along the edges of the serration, the convection velocities are studied through space-time correlations (cross-correlations), defined as

$$R_{p'_i p'_j}(x_i, x_j, y, \tau) = \frac{\overline{p'_i(x_i, t)p'_j(x_j, t + \tau)}}{p'_{rms}(x_i, t)p'_{rms}(x_j, t)}, \quad (4)$$

where p'_i and p'_j are the wall pressure fluctuations from transducers located at two positions, namely, x_i and x_j , separated by the stream-wise distance ξ . The delay between the peaks of the cross correlation curves indicates the time required for flow structures to travel across the distance between the transducers (ξ) to generate a similar surface pressure signature. This time delay and the separation distance is then used to calculate the convection velocity.^{56,57}

Figure 12 presents the contour plots of the calculated cross correlation functions along stream-wise direction $0.15 < x'/2h < 0.92$ for both serrated (SER) and straight trailing-edge (STR) cases. The results for the centerline transducers are displayed in Figs. 12(a)–12(d) and show the contour plots for the transducers along the edge of the serration. The vertical axis of the plots represents the spatial domain ($x'/2h$), and the horizontal axis represents the normalized time delay ($\tau U_\infty / 2h$). The ridges in the contour plots depict how the highly correlated structures move from upstream toward the trailing-edge with time.

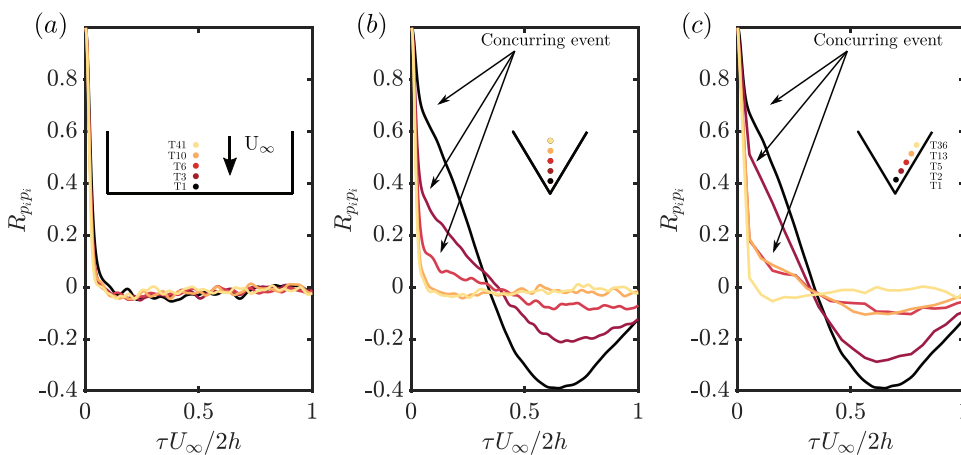


FIG. 11. Auto-correlation functions of wall pressure fluctuations as a function of $\tau^* = \tau U_\infty / 2h$ for transducers along (a) the centerline of straight trailing-edge (T1, T3, T10, T16, and T41), (b) the centerline of serrated trailing-edge (T1, T3, T6, T10, and T16), and (c) the edge of the serration (T1, T2, T5, T13, and T36).

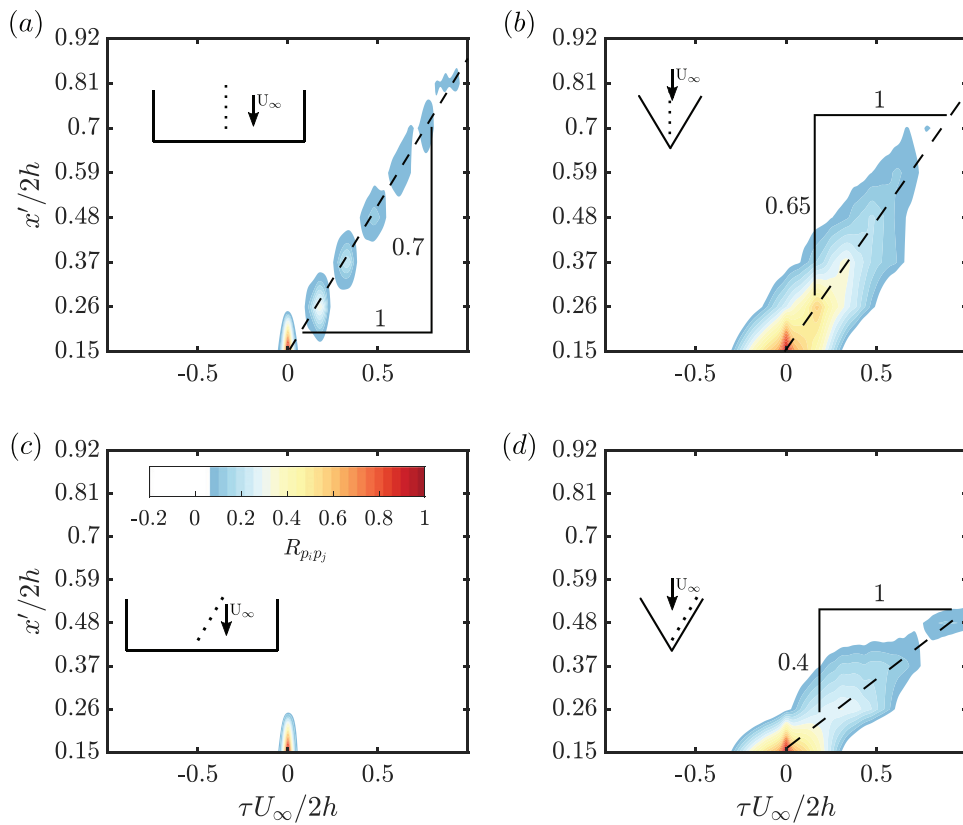


FIG. 12. Contours of the cross correlation function, R_{p_i, p_j} , over the serrated region with respect to transducer T1 along (a) the centerline of straight trailing-edge, (b) the centerline of serrated trailing-edge, (c) the edge of the serration on straight trailing-edge, and (d) the edge of the serration on serrated trailing-edge.

Therefore, the highly correlated region’s slope represents the convection velocity at the trailing-edge. For the straight trailing-edge, the estimated convection velocity at the centerline is approximately $0.70 U_\infty$, which is consistent with the literature.^{8,58,59} The presence of the serration slightly reduces the convection velocity at the centerline to approximately $0.65 U_\infty$, as shown in Fig. 12(b). However, the magnitude of and the temporal extent of the correlation is significantly higher for the serration case. To shed more light on the flow structures along the serration edge, the cross correlation is also estimated using the data from transducers along the serration edge. The results suggest a convection path along the edge of the serration with a significantly high correlation magnitude. However, the observed convection path exhibit significantly lower velocities compared to the centerline results ($0.4 U_\infty$). Moreover, there is no discernible convection for the straight trailing-edge case for the corresponding angled line of transducers. These observations are consistent with the literature²¹ and corroborate the presence of vortical structures along the serration edges. In addition, considering the analytical prediction models in the literature, the frozen turbulence assumption seems to be not fully valid as the turbulence structures, the velocity and the direction they are convected in are affected by the serration’s presence.

E. Pressure-velocity coherence

To have a better understanding of the relationship between the surface pressure fluctuations and the velocity field, a velocity-pressure

coherence ($\gamma_{p'uw}^2$) study was carried out. The velocity-pressure coherence is defined as

$$\gamma_{p'uw}^2(f) = \frac{|\phi_{p'uw}(f)|^2}{|\phi_{p'p'}(f)||\phi_{u'u'}(f)|} \left(\frac{u_{rms}}{U_\infty} \right)^2, \tag{5}$$

where $\gamma_{p'uw}^2(f)$ represents the magnitude-squared coherence calculated between a pressure and velocity signal, and $\phi_{p'u'}$ denotes the cross-power spectral density spectrum between those signals. The magnitude-squared coherence is corrected with a normalization factor following Zang *et al.*⁶⁰ in order to eliminate any spurious regions of elevated correlation at the transition region from boundary layer to free-stream flow.

Figure 13 presents the results for the corrected magnitude-squared coherence between the wall pressure signal and the velocity signal obtained from hot-wire measurements over the transducer locations T36 (a, b), T13 (c, d), and T1 (e, f), for both the straight (STR) and serrated (SER) trailing-edge cases. Schematics showing the location of the measurement are also illustrated in each row to ease the interpretation of the results. At the upstream location, T36, a strong coherence is observed below $y'/\delta_o < 0.5$ for both STR and SER cases. The highly correlated region below $f=200$ Hz is slightly stronger for the STR case. Moreover, although the correlated regions’ spatial extent is similar around the mid-frequencies, the STR case exhibits slightly higher coherence values. The coherence between the pressure and velocity is apparent until $f=4000$ Hz. Over transducer T13, at $x'/2h = 0.59$ and $z/2h = -0.24$, the effect of the serration on the

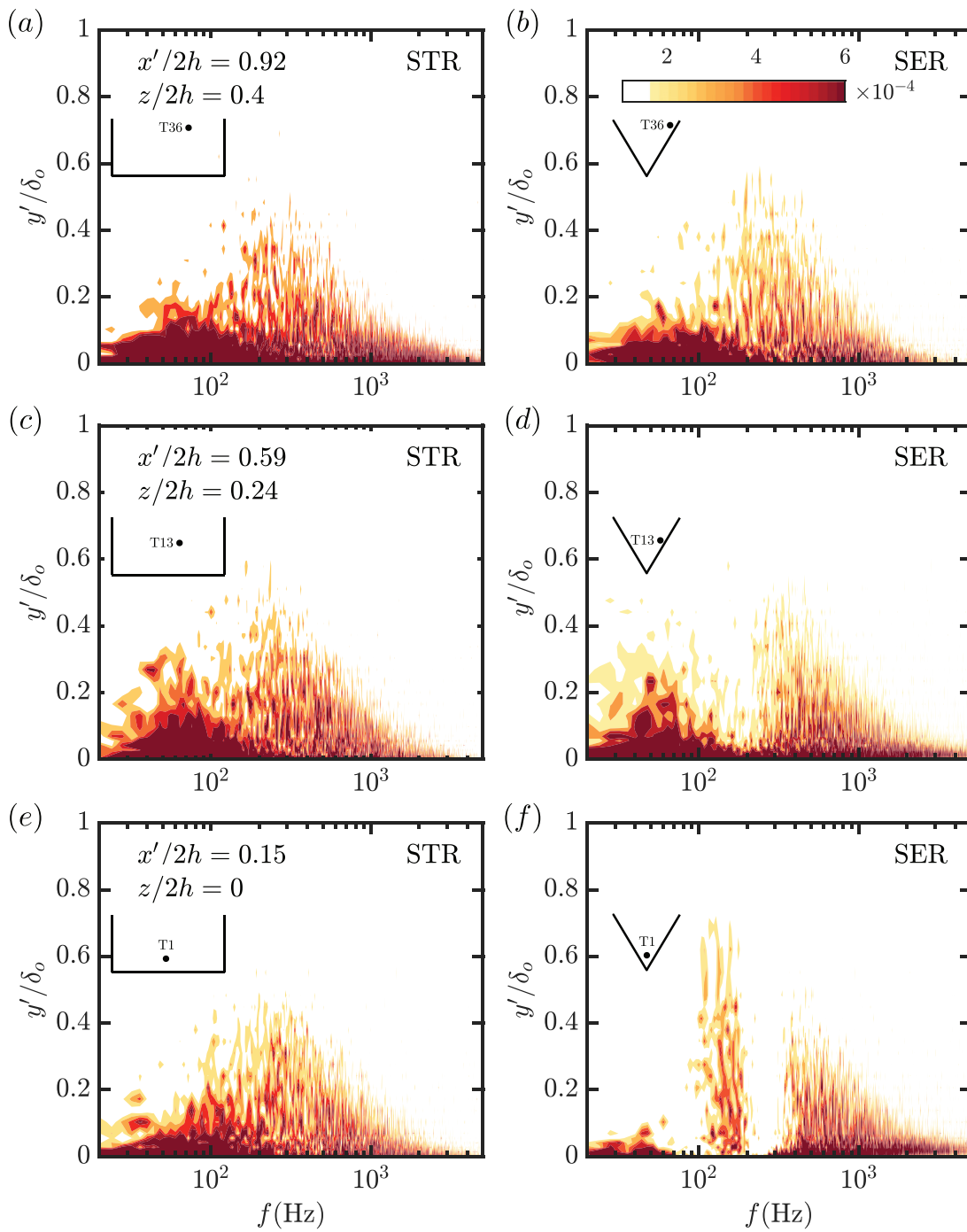


FIG. 13. Contours of the velocity-pressure coherence, $\gamma_{pv}^2(f)$ at locations (a) and (b) T36, (c) and (d) T13, and (e) and (f) T1 for STR and SER cases, respectively.

flow field becomes more apparent. For the STR case, the coherence results are similar to that of upstream location, T36. However, the coherence results for the SER case suggest a sharp decrease at around $150 < f < 400$ Hz compared to the results of both the STR case and upstream location of the SER case. Recalling the results of the energy spectra of the

pressure fluctuations, Fig. 6, it is interesting to note that the coherence loss partially occurs over the spectral band where the energy content of the surface pressure fluctuations increases significantly.

Further downstream, the coherence results for the STR case and transducer T1 ($x'/2h = 0.15$ and $z'/2h = 0$) suggest a loss of

coherence between pressure and velocity fluctuations for $f < 100$ Hz. The results of the SER case exhibit an emergence of two phenomena at this location. First, the reduction observed at around $150 < f < 400$ Hz for T13 results can be observed for this case as well as with a broadened bandwidth. At this location, the spectral band of reduced coherence overlaps with the spectral band of increased energy content of the surface pressure fluctuations. In addition, the broadband coherence below $f = 400$ Hz has almost vanished, with a small island of coherence below $f < 50$ Hz for $y'/\delta_0 < 0.05$. Second, a region of coherence has emerged at approximately $f = 150$ Hz, with a spatial extent up to $y'/\delta_0 = 0.8$. This new narrowband coherence island may be the foot print of highly coherent structures generated on the serration edges, which amalgamate at the tip of the serration.

IV. CONCLUSION

An extensive experimental study was performed to explore and understand the effect of the hydrodynamic field and scattering of the pressure waves on the noise reduction performance of a robust trailing-edge serration. Although the employed serration geometry deviates from the optimal serration geometry descriptions in the literature, the results point toward the possibility of noise attenuation by utilizing robust and large scale serrations. The beamforming results suggest that the serration achieves a noise reduction of approximately 4 dB across the measured spectra. Moreover, the associated flow field studies demonstrated some interesting results regarding the flow field structures above a serrated trailing-edge. Despite the lack of difference between the results of serrated and straight trailing-edges in terms of the mean pressure and velocity quantities, the energy spectra of the surface pressure fluctuations show a significant change. The energy spectra of the unsteady surface pressure fluctuations show an increase along the serration edge compared to the straight trailing-edge case, a low-frequency energy increase associated with a hydrodynamic event developing along the edges of the serration. The estimated convection velocities suggest a slight decrease due to the presence of the serration along the centerline. Moreover, the results also point toward a convection path along the edge of the serration with a markedly lower calculated velocities. The estimated integral-length scale at the center plane of the serration demonstrates no significant change between the STR and SER case at high frequencies. However, at low frequencies, where the dominant hydrodynamic phenomenon occurs, the estimated length scale displays a pronounced increase. Despite the presence of the strong hydrodynamic field at low frequencies for the serrated trailing-edge, a phase change was observed along the serration, which may indicate the presence of destructive interference.

In conclusion, the results of this experimental investigation demonstrate that a noise reduction is achievable for a broad range of frequencies with large scale serrations. The limitations of the beamforming technique at low frequencies avoid observing the far-field effect for $f < 600$ Hz, where strong hydrodynamics events are observed. Despite the strong hydrodynamics field, i.e., increase in the energy of surface pressure fluctuations at low frequencies, a phase difference of the pressure waves along the serration exist, which may be interpreted as the footprint of generation of the destructive interference. Exploring the underpinning physical mechanism of noise reduction and obtaining a comprehensive understanding of the capabilities of serrations at low frequencies may require high-fidelity numerical

simulations, which may provide a simultaneous data set for both near-field and far-field quantities.

ACKNOWLEDGMENTS

The first author would like to acknowledge the financial support of EPSRC (Engineering and Physical Sciences Research Council) via Grant No. EP/S013024/1. The second author would like to acknowledge the financial support through an EPSRC DTP grant. In addition, the authors would like thank Dr. Bin Zang for his contribution in beamforming analysis and Dr. Xiao Liu for her valuable contributions in manufacturing the rig.

DATA AVAILABILITY

The data that support the findings of this study are available from the corresponding author upon reasonable request.

REFERENCES

- ¹WHO, *Environmental Noise Guidelines for the European Region* (World Health Organization Regional Office for Europe, Denmark, 2018).
- ²ACARE, *Flightpath 2050—Europe's Vision for Aviation* (Publications Office of the European Union, Luxembourg 2011).
- ³S. Oerlemans, "Reduction of wind turbine noise using blade trailing edge devices," in 22nd AIAA/CEAS Aeroacoustics Conference, Lyon, France, Paper No. AIAA-2016-3018 (2016).
- ⁴T. Brooks, D. Pope, and M. Marcolini, "Airfoil self-noise and prediction," Report No. L-16528 (National Aeronautics and Space Administration, Office of Management, 1989).
- ⁵M. Howe, "A review of the theory of trailing edge noise," *J. Sound Vib.* **61**, 437–465 (1978).
- ⁶J. E. Ffowcs Williams and D. L. Hawkings, "Sound generation by turbulence and surfaces in arbitrary motion," *Philos. Trans. R. Soc. London, Ser. A* **264**, 321–342 (1969).
- ⁷R. Amiet, "Acoustic radiation from an airfoil in a turbulent stream," *J. Sound Vib.* **41**, 407–420 (1975).
- ⁸R. Amiet, "Noise due to turbulent flow past a trailing edge," *J. Sound Vib.* **47**, 387–393 (1976).
- ⁹D. M. Chase, "Noise radiated from an edge in turbulent flow," *AIAA J.* **13**, 1041–1047 (1975).
- ¹⁰M. Szóke, D. Fisaletti, and M. Azarpeyvand, "Uniform flow injection into a turbulent boundary layer for trailing edge noise reduction," *Phys. Fluids* **32**, 085104 (2020).
- ¹¹M. Szóke, D. Fisaletti, and M. Azarpeyvand, "Influence of boundary layer flow suction on trailing edge noise generation," *J. Sound Vib.* **475**, 115276 (2020).
- ¹²A. Inasawa, C. Ninomiya, and M. Asai, "Suppression of tonal trailing-edge noise from an airfoil using a plasma actuator," *AIAA J.* **51**, 1695–1702 (2013).
- ¹³T. Geyer, E. Sarradj, and C. Fritzsche, "Measurement of the noise generation at the trailing edge of porous airfoils," *Exp. Fluids* **48**, 291–308 (2010).
- ¹⁴S. Showkat Ali, M. Azarpeyvand, and C. Ilário da Silva, "Trailing-edge flow and noise control using porous treatments," *J. Fluid Mech.* **850**, 83–119 (2018).
- ¹⁵A. Rubio Carpio, R. Merino Martínez, F. Avallone, D. Ragni, M. Snellen, and S. van der Zwaag, "Experimental characterization of the turbulent boundary layer over a porous trailing edge for noise abatement," *J. Sound Vib.* **443**, 537–558 (2019).
- ¹⁶E. J. G. Arcondoulis, T. F. Geyer, and Y. Liu, "An investigation of wake flows produced by asymmetrically structured porous coated cylinders," *Phys. Fluids* **33**, 037124 (2021).
- ¹⁷C. Teruna, F. Avallone, D. Ragni, and D. Casalino, "On the noise reduction of a porous trailing edge applied to an airfoil at lifting condition," *Phys. Fluids* **33**, 055132 (2021).
- ¹⁸L. Bowen, A. Celik, M. Azarpeyvand, and C. R. I. da Silva, "On the use of tailored permeable surfaces for turbulence interaction noise control," in AIAA Aviation 2020 Forum, Paper No. AIAA 2020-2530 (2020).

- ¹⁹M. S. Howe, "Noise produced by a sawtooth trailing edge," *J. Acoust. Soc. Am.* **90**, 482–487 (1991).
- ²⁰F. Avallone, S. Pröbsting, and D. Ragni, "Three-dimensional flow field over a trailing-edge serration and implications on broadband noise," *Phys. Fluids* **28**, 117101 (2016).
- ²¹T. P. Chong and A. Vathylakis, "On the aeroacoustic and flow structures developed on a flat plate with a serrated sawtooth trailing edge," *J. Sound Vib.* **354**, 65–90 (2015).
- ²²S. L. Prigent, O. R. H. Buxton, and P. J. K. Bruce, "Coherent structures shed by multiscale cut-in trailing edge serrations on lifting wings," *Phys. Fluids* **29**, 075107 (2017).
- ²³Y. Shi and W. Kollmann, "Improved delayed detached eddy simulation of a porous wavy trailing edge," *Phys. Fluids* **33**, 055128 (2021).
- ²⁴N. Thomareis and G. Papadakis, "Effect of trailing edge shape on the separated flow characteristics around an airfoil at low Reynolds number: A numerical study," *Phys. Fluids* **29**, 014101 (2017).
- ²⁵A. Celik, Y. Mayer, and M. Azarpeyvand, "An experimental aeroacoustic study on serrated trailing-edge geometries and flow misalignment effects," in AIAA Aviation 2020 Forum, Paper AIAA No. 2020-2518 (2020).
- ²⁶S. Moreau, M. Sanjosé, B. Lyu, and L. J. Ayton, "Analytical, numerical and experimental investigation of trailing-edge noise reduction on a controlled diffusion airfoil with serrations," in 25th AIAA/CEAS Aeroacoustics Conference, Delft, The Netherlands, Paper No. AIAA-2019-2450 (2019).
- ²⁷A. Afshari, M. Azarpeyvand, A. A. Dehghan, M. Szöke, and R. Maryami, "Trailing-edge flow manipulation using streamwise finlets," *J. Fluid Mech.* **870**, 617–650 (2019).
- ²⁸M. Gruber, P. Joseph, and T. Chong, "On the mechanisms of serrated airfoil trailing edge noise reduction," in 17th AIAA/CEAS Aeroacoustics Conference (32nd AIAA Aeroacoustics Conference), Portland, Oregon, Paper No. AIAA-2011-2781 (2011).
- ²⁹D. J. Moreau and C. J. Doolan, "Noise-reduction mechanism of a flat-plate serrated trailing edge," *AIAA J.* **51**, 2513–2522 (2013).
- ³⁰F. Avallone, W. C. P. van der Velden, D. Ragni, and D. Casalino, "Noise reduction mechanisms of sawtooth and combed-sawtooth trailing-edge serrations," *J. Fluid Mech.* **848**, 560–591 (2018).
- ³¹M. Gruber, P. Joseph, and T. P. Chong, "Experimental investigation of airfoil self noise and turbulent wake reduction by the use of trailing edge serrations," in 16th AIAA/CEAS Aeroacoustics Conference, Stockholm, Sweden, Paper No. AIAA-2010-3803 (2010).
- ³²L. E. Jones and R. D. Sandberg, "Acoustic and hydrodynamic analysis of the flow around an aerofoil with trailing-edge serrations," *J. Fluid Mech.* **706**, 295–322 (2012).
- ³³H. Cao, M. Zhang, C. Cai, and Z. Zhang, "Flow topology and noise modeling of trailing edge serrations," *Appl. Acoust.* **168**, 107423 (2020).
- ³⁴M. B. R. Gelot and J. W. Kim, "Effect of serrated trailing edges on aerofoil tonal noise," *J. Fluid Mech.* **904**, A30 (2020).
- ³⁵B. Lyu, M. Azarpeyvand, and S. Sinayoko, "Prediction of noise from serrated trailing edges," *J. Fluid Mech.* **793**, 556–588 (2016).
- ³⁶Y. D. Mayer, B. Lyu, H. K. Jawahar, and M. Azarpeyvand, "A semi-analytical noise prediction model for airfoils with serrated trailing edges," *Renewable Energy* **143**, 679–691 (2019).
- ³⁷S. Oerlemans, M. Fisher, T. Maeder, and K. Kögler, "Reduction of wind turbine noise using optimized airfoils and trailing-edge serrations," *AIAA J.* **47**, 1470–1481 (2009).
- ³⁸C. A. León, D. Ragni, S. Pröbsting, F. Scarano, and J. Madsen, "Flow topology and acoustic emissions of trailing edge serrations at incidence," *Exp. Fluids* **57**, 91 (2016).
- ³⁹F. Avallone, W. van der Velden, and D. Ragni, "Benefits of curved serrations on broadband trailing-edge noise reduction," *J. Sound Vib.* **400**, 167–177 (2017).
- ⁴⁰C. A. León, R. Merino-Martínez, S. Pröbsting, D. Ragni, and F. Avallone, "Acoustic emissions of semi-permeable trailing edge serrations," *Acoust. Australia* **46**, 111–117 (2018).
- ⁴¹M. Herr and W. Dobrzynski, "Experimental investigations in low-noise trailing edge design," *AIAA J.* **43**, 1167–1175 (2005).
- ⁴²D. Ragni, F. Avallone, W. C. P. van der Velden, and D. Casalino, "Measurements of near-wall pressure fluctuations for trailing-edge serrations and slits," *Exp. Fluids* **60**, 111–117 (2019).
- ⁴³T. P. Chong, A. Vathylakis, P. F. Joseph, and M. Gruber, "Self-noise produced by an airfoil with nonflat plate trailing-edge serrations," *AIAA J.* **51**, 2665–2677 (2013).
- ⁴⁴T. Chong, P. Joseph, and M. Gruber, "Airfoil self noise reduction by non-flat plate type trailing edge serrations," *Appl. Acoust.* **74**, 607–613 (2013).
- ⁴⁵Y. D. Mayer, H. K. Jawahar, M. Szöke, S. A. S. Ali, and M. Azarpeyvand, "Design and performance of an aeroacoustic wind tunnel facility at the University of Bristol," *Appl. Acoust.* **155**, 358–370 (2019).
- ⁴⁶E. Sarraj and G. Herold, "A python framework for microphone array data processing," *Appl. Acoust.* **116**, 50–58 (2017).
- ⁴⁷G. M. Corcos, "The structure of the turbulent pressure field in boundary-layer flows," *J. Fluid Mech.* **18**, 353–378 (1964).
- ⁴⁸R. Merino-Martínez, P. Sijtsma, A. R. Carpio, R. Zamponi, S. Luesuthiviboon, A. M. Malgoezar, M. Snellen, C. Schram, and D. G. Simons, "Integration methods for distributed sound sources," *Int. J. Aeroacoust.* **18**, 444–469 (2019).
- ⁴⁹M. Howe, "Aerodynamic noise of a serrated trailing edge," *J. Fluids Struct.* **5**, 33–45 (1991).
- ⁵⁰A. Fischer, F. Bertagnoli, W. Z. Shen, J. Madsen, H. A. Madsen, C. Bak, W. Devenport, and N. Intarapet, "Wind tunnel test of trailing edge serrations for the reduction of wind turbine noise," in Inter Noise, Melbourne, Australia (2014).
- ⁵¹P. Zhou, Q. Liu, S. Zhong, Y. Fang, and X. Zhang, "A study of the effect of serration shape and flexibility on trailing edge noise," *Phys. Fluids* **32**, 127114 (2020).
- ⁵²H. Kamliya Jawahar, S. A. Showkat Ali, and M. Azarpeyvand, "Serrated slat cusp for high-lift device noise reduction," *Phys. Fluids* **33**, 015107 (2021).
- ⁵³P. Welch, "The use of fast Fourier transform for the estimation of power spectra: A method based on time averaging over short, modified periodograms," *IEEE Trans. Audio Electroacoust.* **15**, 70–73 (1967).
- ⁵⁴M. Goody, "Empirical spectral model of surface pressure fluctuations," *AIAA J.* **42**, 1788–1794 (2004).
- ⁵⁵S. Glegg and D. Devenport, *Aeroacoustics of Low Mach Number Flows*, 1st ed. (Elsevier Inc., New York, 2017), Chap. 8.
- ⁵⁶J. F. Largeau and V. Moriniere, "Wall pressure fluctuations and topology in separated flows over a forward-facing step," *Exp. Fluids* **42**, 21 (2006).
- ⁵⁷A. Celik, J. L. Bowen, and M. Azarpeyvand, "Effect of trailing-edge bevel on the aeroacoustics of a flat-plate," *Phys. Fluids* **32**, 105116 (2020).
- ⁵⁸J. C. Yu and C. K. W. Tam, "Experimental investigation of the trailing edge noise mechanism," *AIAA J.* **16**, 1046–1052 (1978).
- ⁵⁹T. Brooks and T. Hodgson, "Trailing edge noise prediction from measured surface pressures," *J. Sound Vib.* **78**, 69–117 (1981).
- ⁶⁰B. Zang, Y. D. Mayer, and M. Azarpeyvand, "A note on the pressure-velocity correlation and coherence normalisation," *Exp. Fluids* **61**, 186 (2020).